



## Novel fluorine-doped cobalt molybdate nanosheets with enriched oxygen-vacancies for improved oxygen evolution reaction activity

Weiwei Xie <sup>a</sup>, Jianhao Huang <sup>a</sup>, Liting Huang <sup>a</sup>, Shipeng Geng <sup>a</sup>, Shuqin Song <sup>a</sup>, Panagiotis Tsiakaras <sup>b,\*</sup>, Yi Wang <sup>a,\*</sup>

<sup>a</sup> The Key Lab of Low-Carbon Chemistry & Energy Conservation of Guangdong Province, PCFM Lab, School of Chemical Engineering and Technology, School of Materials Science and Engineering, Sun Yat-sen University, Guangzhou 510275, China

<sup>b</sup> Laboratory of Alternative Energy Conversion Systems, Department of Mechanical Engineering, School of Engineering, University of Thessaly, 1 Sekeri Str., Pedion Areos, 38834 Volos, Greece



### ARTICLE INFO

#### Keywords:

Oxygen evolution reaction  
Fluorine-engineering  
Fluorine-doped CoMoO<sub>4</sub>  
Oxygen vacancies  
DFT

### ABSTRACT

Herein, we have synthesized fluorine-doped cobalt molybdate (F-CoMoO<sub>4</sub>) nanosheet arrays on graphite felt (GF) to efficiently promote the oxygen evolution reaction (OER) kinetics. Experimental results show that F-CoMoO<sub>4</sub> has two significant effects: 1) inducing rich oxygen vacancies, and 2) optimizing the electronic configuration of CoMoO<sub>4</sub>, which is beneficial for exposure of active sites. The as-obtained F-CoMoO<sub>4-x</sub>-2@GF electrocatalyst exhibits lower OER overpotential of 256 mV at 10 mA cm<sup>-2</sup> with a small Tafel slope of 64.4 mV dec<sup>-1</sup> in alkaline solution, resulting in a nearly 100 mV of OER catalytic activity enhancement compared with that of pure CoMoO<sub>4</sub>. DFT results reveal that the change of Mo 4d state reduces the band-gap and increases the electrical conductivity of CoMoO<sub>4</sub>, thus optimizing its intrinsic activity. The synthesis strategy used in this work may provide some ideas for enhancing the electrical conductivity of other transition metal oxides (TMOs).

### 1. Introduction

The sustainable development of human beings needs endless amounts of energy that can hardly be covered by traditional energy sources (coal, petroleum and gasoline). Therefore, the exploration of efficient and sustainable forms of energy is essential [1,2]. Hydrogen energy has received extensive attention and been considered as promising energy source due to its environmental friendliness, high heat of combustion and convenient chemical preparation methods [3]. Among different hydrogen production technologies, the electrocatalytic water splitting (EWS) has attracted much attention due to its moderate chemical reaction, convenient operation and high hydrogen production efficiency [4,5]. EWS includes two half reactions: hydrogen evolution reaction (HER) and oxygen evolution reaction (OER). Between them, the OER seriously impedes the overall hydrogen production efficiency due to its sluggish kinetics associated with the complicated 4-electron transfer, which leads to a much higher cell voltage than 1.23 V [6]. Therefore, the effective electrocatalysts are intended to decrease the OER overpotential, thereby promoting the efficiency of EWS and reducing the loss of power. So far, precious metal electrocatalysts, such

as RuO<sub>2</sub> or IrO<sub>2</sub>, are still in the mainstream due to their high OER performance. However, their scarcity, high cost and low stability are the major obstacles to widespread applications in commercial water splitting [7,8]. Therefore, the exploration and development of non-precious metal catalysts with high efficiency, abundant reserves, low price, and excellent durability has recently become the focus of OER investigations [9,10].

The last years, transition metal oxides (TMOs), such as Fe<sub>2</sub>O<sub>3</sub> [11], MnO<sub>2</sub> [12], NiO [13], Zn<sub>x</sub>Co<sub>3-x</sub>O<sub>4</sub> [14], NiMoO<sub>4</sub> [15] and Co<sub>3</sub>O<sub>4</sub> [16], have been widely used as OER electrocatalysts on account of their abundant reserves, high activity and variable components [17–20]. Actually, pure TMOs usually show poor OER catalytic activity [21,22]. In this regard, various modified strategies have been adopted to enhance their OER catalytic activity. Among them: 1) elemental doping can adjust electronic structure and improve intrinsic activity of catalysts [23]; 2) oxygen vacancies enhance the catalytic performance of OER by activating inert active sites [24]; 3) regulating favorable crystal surfaces can help to improve the OER catalytic performance [25], and 4) the construction of heterogeneous structures can effectively increase the amount of active sites and accelerate charge diffusion and ion transfer

\* Corresponding authors.

E-mail addresses: [tsiak@uth.gr](mailto:tsiak@uth.gr) (P. Tsiakaras), [wangyi76@mail.sysu.edu.cn](mailto:wangyi76@mail.sysu.edu.cn) (Y. Wang).

[26]. At present, heteroatom doping and vacancy engineering are the main research fields in defect engineering [27]. Non-metal elemental doping (P, N, and S) is a convenient and efficient method. Wang et al. reported that introducing P into  $\text{Co}_3\text{O}_4$  by high-temperature calcination could enhance the overall activity of water-splitting [28]. Xu et al. improved the electronic conductivity through N doping to enhance the OER activity of  $\text{Co}_3\text{O}_4$  nanosheets [29]. However, the conventional non-metal elemental doping does not improve OER performance significantly, which may hinder its further development prospect in practical applications [30]. It is expected that the introduction of a particular non-metal element may improve the electronic conductivity of TMOs, thus further enhancing their catalytic activity. In addition, oxygen vacancies can improve catalytic performance by providing additional active sites. Generally, hydrogen/ $\text{NaBH}_4$  reduction is the most common strategy in the formation of oxygen vacancies in the metal oxide crystal structures [31].

Interestingly, fluorine (F) element, as the most electronegative element (4.0) may not only induce much more efficient regulation for the electronic structure, but also lead to richer oxygen vacancies or defects in materials for favorable catalysis with respect to the other non-metal elements. He et al. reasonably introduced F ions into  $\text{Ni}_3\text{S}_2$  nanosheet arrays, which positively modified the electronic structure and thus enhanced the HER performance [32]. What's more exciting was that Xu et al. introduced F into CoP nanosheets through calcination of ammonium fluoride and meanwhile rich P vacancies were generated, leading to a great improvement in HER performance [33]. F-induced construction of double-defect engineering to improve catalytic performance may be applied in other energy conversion reactions such as OER.

Inspired by the above discussion, a convenient strategy has been adopted to synthesize a typical  $\text{ABO}_4$ -type material,  $\text{CoMoO}_4$  nanosheet arrays on graphite felt ( $\text{CoMoO}_4@\text{GF}$ ), by using the hydrothermal method. Then, with F introduction into  $\text{CoMoO}_4$ , the surface structure can be regulated, and simultaneously rich oxygen vacancies can be produced on the surface of  $\text{F-CoMoO}_{4-x}2@\text{GF}$  (the optimized sample in this work), as confirmed by both XPS and EPR results. The theoretical calculation results reveal that the fluorine-engineering of  $\text{CoMoO}_4$  can regulate its electronic structure, reduce the band-gap and thus promote the OER kinetic process. The optimal catalyst,  $\text{F-CoMoO}_{4-x}2@\text{GF}$ , shows good OER activity with 256 mV overpotential at  $10 \text{ mA cm}^{-2}$ , which is better than that of most advanced TMOs electrocatalysts. This is an effective doping method to enhance the catalytic OER performance of TMOs. It is believed that the fluorine-engineering strategy presented in this work may be extended to modulate other TMOs with improved catalytic activity.

## 2. Experimental section

### 2.1. Materials and methods

Graphite Felt (GF) was purchased from Jing Long TeTan Materials Corporation.  $\text{Na}_2\text{MoO}_4 \cdot 2\text{H}_2\text{O}$  (99.0%) and anhydrous  $\text{C}_2\text{H}_5\text{OH}$  were purchased from Shanghai Chemical Reagents Corporation.  $\text{Co}(\text{NO}_3)_2 \cdot 6\text{H}_2\text{O}$  (99.0%) and HCl (37 wt%) were obtained from Tianjin Chemical Reagents. All of the above chemicals were of analytical grade and directly used without any further treatment.

### 2.2. Synthesis of $\text{CoMoO}_4@\text{GF}$

Typically, bulk GF was cut into small pieces ( $2.0 \text{ cm} \times 3.0 \text{ cm}$ ). Then, they were successively sonicated in HCl (12.0 mol/L),  $\text{C}_2\text{H}_5\text{OH}$ , and deionized (DI) water for 10 min each step, followed by transferring to a vacuum drying oven at  $60^\circ\text{C}$  for 6 h. For the in-situ growing of  $\text{CoMoO}_4$  on GF, specifically, 0.9680 g  $\text{Na}_2\text{MoO}_4 \cdot 2\text{H}_2\text{O}$  and 0.6000 g urea were dissolved in 70.0 mL deionized (DI) water under ultrasonication. Meanwhile, 1.1640 g  $\text{Co}(\text{NO}_3)_2 \cdot 6\text{H}_2\text{O}$  was also dissolved in 80.0 mL DI water, then mixed with the above solution and kept stirred for 15 min.

The obtained solution (35.0 mL) and a piece of prepared GF were transferred into the Teflon-lined stainless-steel autoclave (50.0 mL), followed by heating at  $160^\circ\text{C}$  for 6 h in an air-dry oven. After naturally cooling down to room temperature, the GF coated with precursors was washed with DI water, and then dried at  $60^\circ\text{C}$  for 10 h. Finally, the obtained materials were calcined at  $400^\circ\text{C}$  for 1 h under flowing  $\text{N}_2$  atmosphere to form  $\text{CoMoO}_4@\text{GF}$ .

### 2.3. Synthesis of $\text{F-CoMoO}_{4-x}2@\text{GF}$

To synthesize  $\text{F-CoMoO}_{4-x}2@\text{GF}$  samples, the Co-Mo precursors and ammonium fluoride ( $\text{NH}_4\text{F}$ ) were each placed in a porcelain boat, in which the boat containing  $\text{NH}_4\text{F}$  was closer to the inlet of the tube furnace. Here, considering that adopting hydrogen fluoride (HF) produced by the  $\text{NH}_4\text{F}$  decomposition is a safer and more convenient way than using HF gas directly,  $\text{NH}_4\text{F}$  was selected as the fluorine source. Subsequently, the sample was heated to  $400^\circ\text{C}$  with a heating rate of  $10^\circ\text{C min}^{-1}$  under flowing  $\text{N}_2$  atmosphere and kept at  $400^\circ\text{C}$  for 1 h. In order to optimize F content in the sample, different amounts of  $\text{NH}_4\text{F}$  (1.00, 2.00, 3.00, and 4.00 g  $\text{NH}_4\text{F}$ ) were used to obtain different F content doped  $\text{CoMoO}_4@\text{GF}$ , and the as-obtained materials were denoted as  $\text{F-CoMoO}_{4-x}2@\text{GF}$  (x represents partially missing oxygen,  $0 < x < 4$ ; n = 1, 2, 3, and 4, representing the feeding weight of  $\text{NH}_4\text{F}$ ). The average loading amount of  $\text{F-CoMoO}_{4-x}2$  was  $\sim 4.26 \text{ mg/cm}^2$ .

## 2.4. Materials characterization

X-ray diffraction (XRD) patterns were acquired using a diffractometer (D-MAX 2200 VPC) from  $10^\circ$  to  $90^\circ$ , equipped with  $\text{Cu K}\alpha$  radiation. Raman spectra were obtained by a HORIBA Jobin Yvon, LabRam HR800 Laser confocal spectrograph. The scanning electron microscopy (SEM) images were taken with Quanta 400FEG microscope, while the transmission electron microscopy (TEM) images were acquired on FEI TECNAI F30 HRTEM. The specific surface area and pore structure distribution were obtained by Brunauer-Emmett-Teller (BET) analysis. X-ray photoelectron spectroscopy (XPS) was performed by the aid of Thermal Fisher Scientific ESCALAB 250 spectrometers. Electron paramagnetic resonance (EPR) test was taken with JES-FA200 A300-10-12.

### 2.5. Electrochemical characterization

All electrochemical data were acquired using an AutoLab electrochemical workstation equipped with a three-electrode system. The as prepared  $\text{CoMoO}_4$  based catalysts loaded on GF were applied as the working electrode.  $\text{Hg}/\text{HgO}$  electrode and graphite sheet were used as the reference and counter electrode, respectively. In the electrochemical tests involved in the present investigation, the geometric area of the working electrode immersed in the electrolyte was  $1.0 \text{ cm} \times 1.0 \text{ cm}$ . All the potentials, tested versus  $\text{Hg}/\text{HgO}$  electrode, were calibrated to the ones versus reversible hydrogen electrode (RHE) according to Eq. (1). Without specification, all potentials in the present work are referred to RHE:

$$E(\text{vs-RHE}) = E(\text{vs-Hg/HgO}) + 0.098 \text{ V} + 0.059 \text{ pH} \quad (1)$$

Linear sweep voltammetry (LSV) was applied in the potential range from 0.924 to 1.924 V. Electrochemical impedance spectroscopy (EIS) was applied in the frequency range of  $10^{-1}$ – $10^5 \text{ Hz}$  at the potential of 1.574 V. The double-layer capacitance ( $C_{dl}$ ) was obtained from the cyclic voltammograms (CVs) with the scan rates of 10, 20, 40, 60, 80, and 100 mV/s from 1.20 to 1.35 V. The stability measurements were carried out by using chronoamperometry. For comparison reasons, commercial  $\text{RuO}_2$  supported on GF electrode ( $\text{RuO}_2@\text{GF}$ ) was fabricated as follows: 80.0  $\mu\text{L}$  Nafion® (5 wt%), 520.0  $\mu\text{L}$   $(\text{CH}_3)_2\text{CHOH}$ , 400.0  $\mu\text{L}$  DI water and 10.0 mg  $\text{RuO}_2$  powder were mixed and sonicated for 30 min. Then, the proper amount of ink (426.0  $\mu\text{L}$ ) was loaded onto GF according to the

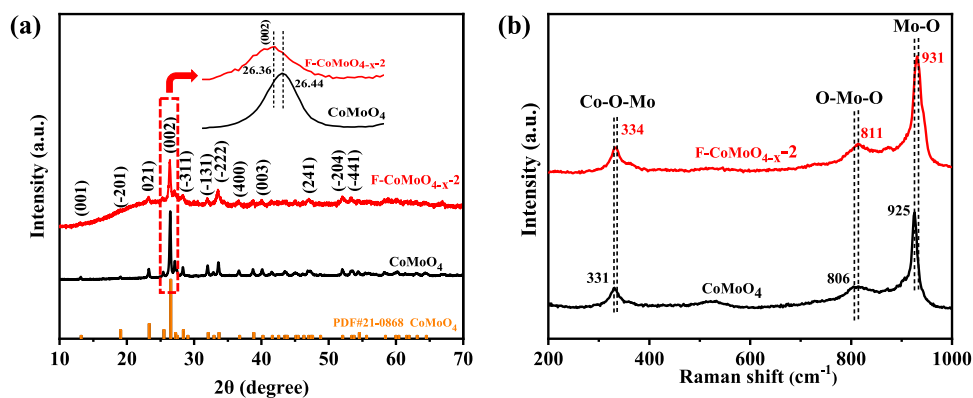


Fig. 1. (a) XRD patterns and (b) Raman spectra of CoMoO<sub>4</sub> and F-CoMoO<sub>4-x-2</sub>.

pre-designed RuO<sub>2</sub> loading.

#### 2.6. Density functional theory calculations

Density functional theory (DFT) calculations were implemented by the aid of Vienna ab initio simulation package (VASP), using the Projected Augmented Wave (PAW) method. In addition, the generalized gradient approximation Perdew-Burke-Ernzerh function was used to describe the electron exchange correlation interaction. The respective Hubbard U values of cobalt and molybdenum were set at 3.32 and 4.38 eV. For electronic structure calculations, the Monkhorst-Pack *k*-point mesh was set to 3 × 3 × 4 for irreducible Brillouin zone. The cutoff energy of the plane wave function was 520 eV. The final force of all relaxed atoms and the consistent convergence accuracy were set as 1.5 × 10<sup>-3</sup> eV Å<sup>-1</sup> and 1.0 × 10<sup>-4</sup> eV, respectively. For the surface free energy

calculation, the CoMoO<sub>4</sub> (002) surface was used to build slabs including three layers and a 15 Å thick vacuum. The top layer was allowed to relax for a minimum energy. A plane-wave cutoff of 400 eV and 2 × 3 × 1 Monkhorst-Pack *k*-point mesh was employed. Besides, the self-consistent convergence accuracy and the convergence criterion for the maximal force on atoms were set as 1 × 10<sup>-6</sup> eV and 0.02 eV Å<sup>-1</sup>.

### 3. Results and discussion

#### 3.1. Materials characterization

A series of F-CoMoO<sub>4-x</sub>@GF electrocatalyst samples have been prepared by a simple hydrothermal synthesis method and calcination (Fig. S1). The specific process has been described above. XRD patterns can analyze phase structure and material composition of the as-

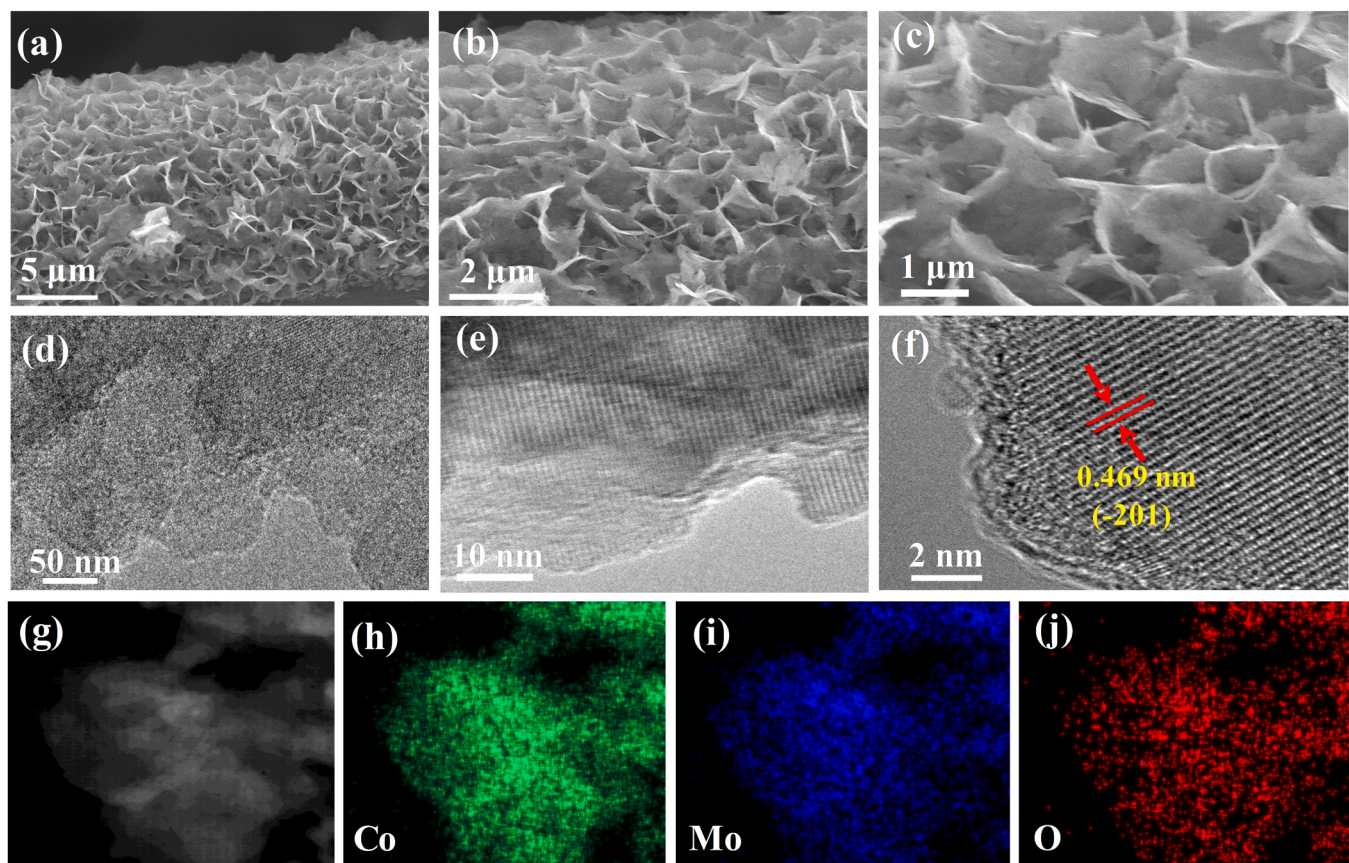
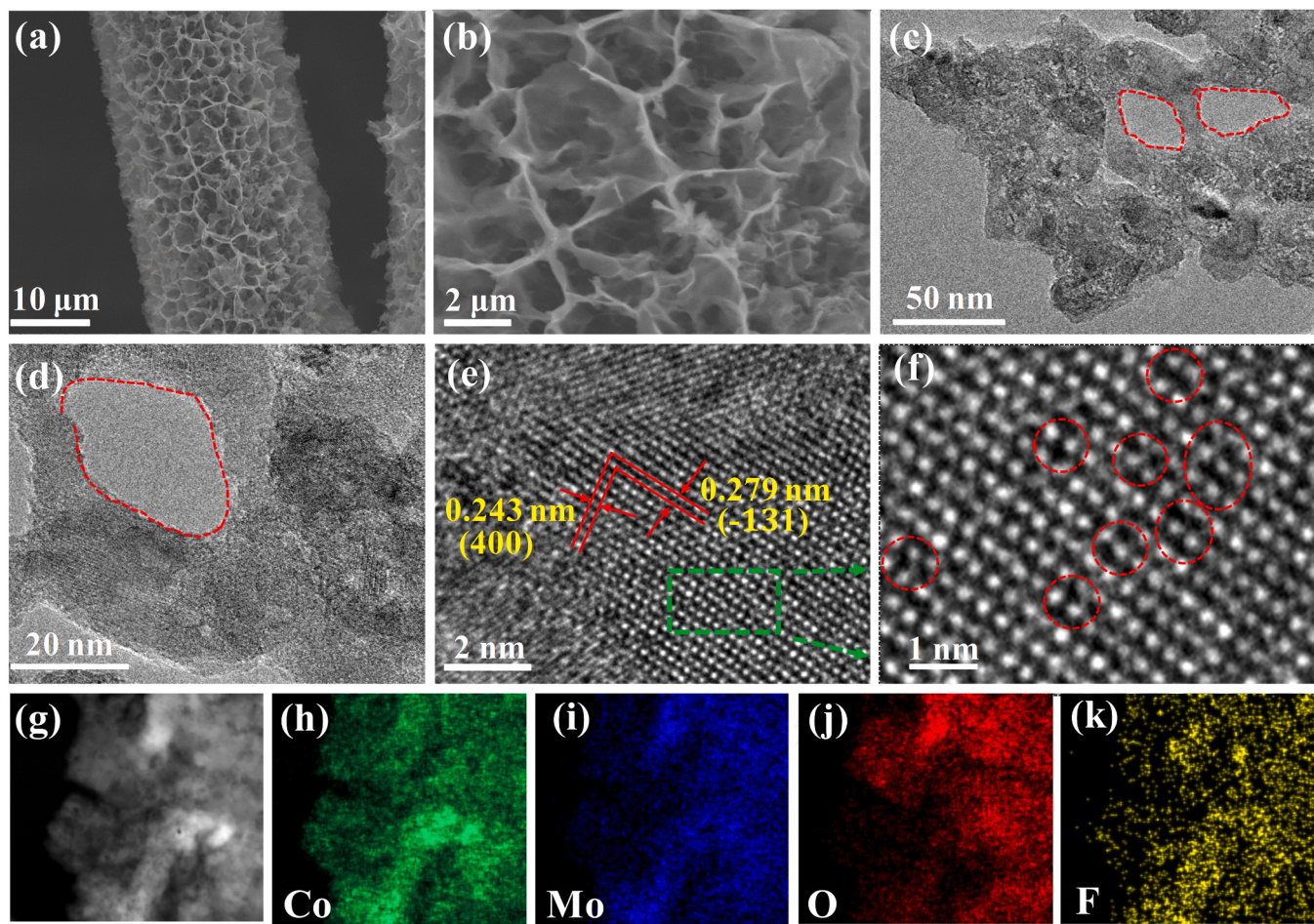


Fig. 2. (a–c) SEM images of CoMoO<sub>4</sub>@GF; (d, e) TEM, (f) HRTEM and (g) SEDTEM images of CoMoO<sub>4</sub>, and (h–j) EDS elemental mapping images of Co, Mo, and O.



**Fig. 3.** (a, b) SEM images of F-CoMoO<sub>4-x</sub>-2@GF; (c, d) TEM images of F-CoMoO<sub>4-x</sub>-2@GF; (e) HRTEM image of F-CoMoO<sub>4-x</sub>-2; (f) enlarged part of the image (e) (the red circles may indicate oxygen vacancies); (g–k) STEM images of F-CoMoO<sub>4-x</sub>-2 and EDS elemental mapping of Co, Mo, O, and F.

synthesized samples. From Fig. S2, it can be seen that the diffraction peaks of CoMoO<sub>4</sub>@GF and pure GF are almost indistinguishable. No obvious diffraction peak signal in CoMoO<sub>4</sub>@GF sample can be observed due to the strong diffraction signal of GF. Therefore, the CoMoO<sub>4</sub> and F-CoMoO<sub>4-x</sub>-n powders were scraped from the GF substrate for further XRD investigation. As clearly seen from Fig. S3, all diffraction peaks belong to the standard XRD patterns of monoclinic CoMoO<sub>4</sub> (PDF#21-0868) [34]. Furthermore, after F-doping, no new diffraction peaks are generated, showing that the fluorine-engineering basically retains the main phase structure of CoMoO<sub>4</sub>. Moreover, by increasing the F doping content, the diffraction peak intensity gradually decreases, implying a lower crystallinity material. This is probably due to the fact that F doping could induce the formation of abundant defects in CoMoO<sub>4</sub>, which will be discussed below. Considering that the electrochemical test results below show that F-CoMoO<sub>4-x</sub>-2@GF exhibits the best electrochemical performance compared with other samples, it will be mainly characterized and analyzed to explore the effect and role of F doping for CoMoO<sub>4</sub>. From Fig. 1a, it can be distinguished that the diffraction peaks of F-CoMoO<sub>4-x</sub>-2@GF are negatively shifted by 0.08°, compared with those of pure CoMoO<sub>4</sub>, indicating a successful F-doping. Furthermore, Raman spectroscopy further confirms these results. Fig. 1b clearly shows that the Raman spectra of F-CoMoO<sub>4-x</sub>-2 and CoMoO<sub>4</sub> basically match in the range of 100–1100 cm<sup>-1</sup>.

The bands at 925, 806 and 331 cm<sup>-1</sup> are attributed to Mo–O, O–Mo–O and Co–O–Mo bonds, respectively. While, the F-CoMoO<sub>4-x</sub>-2 shifts to a higher wavenumber by 3–6 cm<sup>-1</sup> with respect to CoMoO<sub>4</sub>. These results reveal the successful introduction of F without obvious change of the phase structure of CoMoO<sub>4</sub>. Interestingly, with F source dosage

increasing, the peak value of F-CoMoO<sub>4-x</sub>-n gradually shifts to a higher wavenumber as clearly seen from Fig. S4, which may be due to the strong electronegativity of F, resulting in a lower length of metal–F bond.

The morphological characteristics of the CoMoO<sub>4</sub> samples can be evaluated by SEM. Fig. 2a–c show the morphology of CoMoO<sub>4</sub> in magnified version. As can clearly be seen, a honeycomb-like nanosheet array has directly grown on the surface of GFs, implying a successful synthesis strategy. The nanosheets structure was further studied by the aid of TEM. According to Fig. 2(d, e), CoMoO<sub>4</sub> exhibits compact nanosheets characteristics, which are consistent with SEM images.

The high-resolution TEM (HRTEM) of CoMoO<sub>4</sub> (Fig. 2f) clearly shows that the spacing between two adjacent lattice fringes of 0.469 nm corresponds to (–201) plane of CoMoO<sub>4</sub>. In the corresponding element mapping displayed in Fig. 2(g–j), it can be distinguished that all three elements (O, Mo and Co) are homogeneously spread over the sample. In addition, the result from the energy-dispersive X-ray spectroscopy (EDX) (seen in Fig. S5a) also confirms the presence of Co, Mo and O elements in the as prepared samples. After F doping, the F-CoMoO<sub>4-x</sub>-2 inherits the features of honeycomb-like nanosheet arrays (Fig. 3(a, b)), which is confirmed by the TEM images seen in Fig. 3(c, d). Interestingly, the porous structure is shown in these images. Moreover, from the HRTEM image (Fig. 3e), it can be distinguished that the lattice fringes of 0.243 and 0.279 nm are referred to the (400) and (–131) crystal plane indices of CoMoO<sub>4</sub>, respectively.

The enlarged area image, displayed in Fig. 3f, shows the presence of defects, which may be oxygen vacancies caused by F introduction. The results from selected area electron diffraction (SAED) reveal the polycrystalline characteristics of F-CoMoO<sub>4-x</sub>-2 (Fig. S6). The corresponding

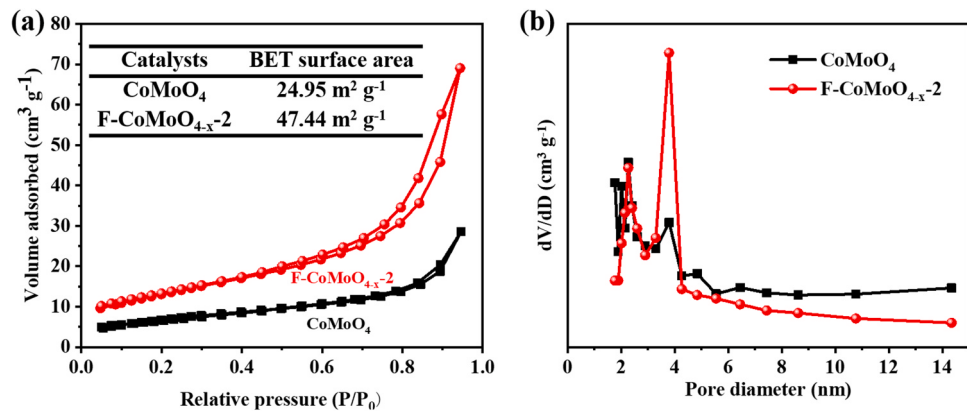


Fig. 4. (a) Nitrogen adsorption/desorption isotherms and (b) pore-size distribution curves for pure CoMoO<sub>4</sub> and F-CoMoO<sub>4-x-2</sub>.

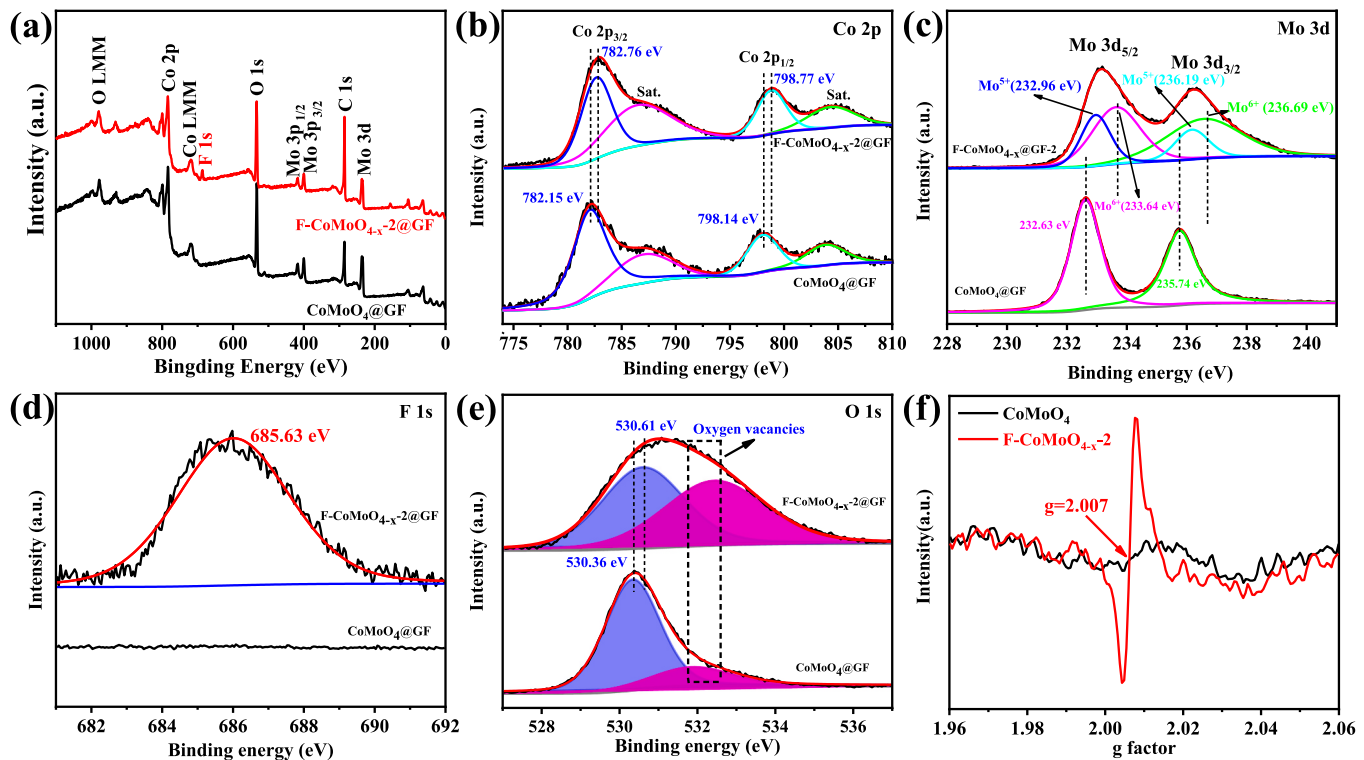


Fig. 5. (a) XPS spectra of CoMoO<sub>4</sub>@GF and F-CoMoO<sub>4-x-2</sub>@GF; (b) Co 2p, (c) Mo 3d, (d) F 1s, and (e) O 1s XPS spectra of CoMoO<sub>4</sub>@GF and F-CoMoO<sub>4-x-2</sub>@GF; (f) EPR spectra of CoMoO<sub>4</sub>@GF and F-CoMoO<sub>4-x-2</sub>@GF.

diffraction rings belong to (−204) and (−311) plane of CoMoO<sub>4</sub>, respectively. These results indicate that the introduction of F into CoMoO<sub>4</sub> can produce amounts of defects and mesoporous structure with no phase transformation. From Fig. 3(g–k), it can be clearly seen the presence of Co, Mo, O and F in the F-CoMoO<sub>4-x-2</sub>, while Fig. S5b confirms that it contains Co, Mo, O and F. To further investigate the porous structure of F-CoMoO<sub>4-x-2</sub>, nitrogen adsorption and desorption isothermal curves were conducted. Fig. 4a shows that both CoMoO<sub>4</sub> and F-CoMoO<sub>4-x-2</sub> present type IV isothermal curves with H<sub>3</sub> type hysteresis, indicating a typical mesoporous characteristic [35].

The BET surface area of CoMoO<sub>4</sub> and F-CoMoO<sub>4-x-2</sub> is calculated to be 24.95 and 47.44 m<sup>2</sup> g<sup>-1</sup>, respectively, indicating that the introduction of F extends the surface area of CoMoO<sub>4</sub>. In the corresponding Barrett–Joyner–Halenda (BJH) pore distribution curve is displayed in Fig. 4 b. The stronger peak intensity of F-CoMoO<sub>4-x-2</sub> is generated at about 4 nm, indicating that the introduction of F causes the generation of most mesopores. This behavior may be due to the reaction of HF gas

produced by NH<sub>4</sub>F at high temperature with part of cobalt molybdate, resulting in the formation of mesopores [36].

XPS can estimate chemical states of the component elements at the electrocatalyst surface. As seen from Fig. 5a, both CoMoO<sub>4</sub>@GF and F-CoMoO<sub>4-x-2</sub>@GF contain Co, Mo and O elements. An obvious diffraction peak at 685.6 eV in F-CoMoO<sub>4-x-2</sub>@GF is judged to be F 1s, indicating the effective and successful introduction of F.

From Fig. 5b, the high-resolution Co 2p spectra of CoMoO<sub>4</sub>@GF show two major peaks at 782.15 and 798.14 eV attributed to Co 2p<sub>3/2</sub> and Co 2p<sub>1/2</sub>, respectively. At the same time, there are two satellite peaks (denoted as “sat.”) at 787.04 and 804.34 eV, belonging to the cobalt oxide species. The above results indicate the presence of Co<sup>2+</sup> oxidation state [37]. Compared with those of CoMoO<sub>4</sub>@GF, the binding energies at Co 2p<sub>3/2</sub> (782.76 eV) and Co 2p<sub>1/2</sub> (798.77 eV) of F-CoMoO<sub>4-x-2</sub>@GF are positively shifted by 0.61 and 0.63 eV, respectively. This proves that the electron density around Co atom is decreased after the fluorine-doping, due to the higher electronegativity of F than

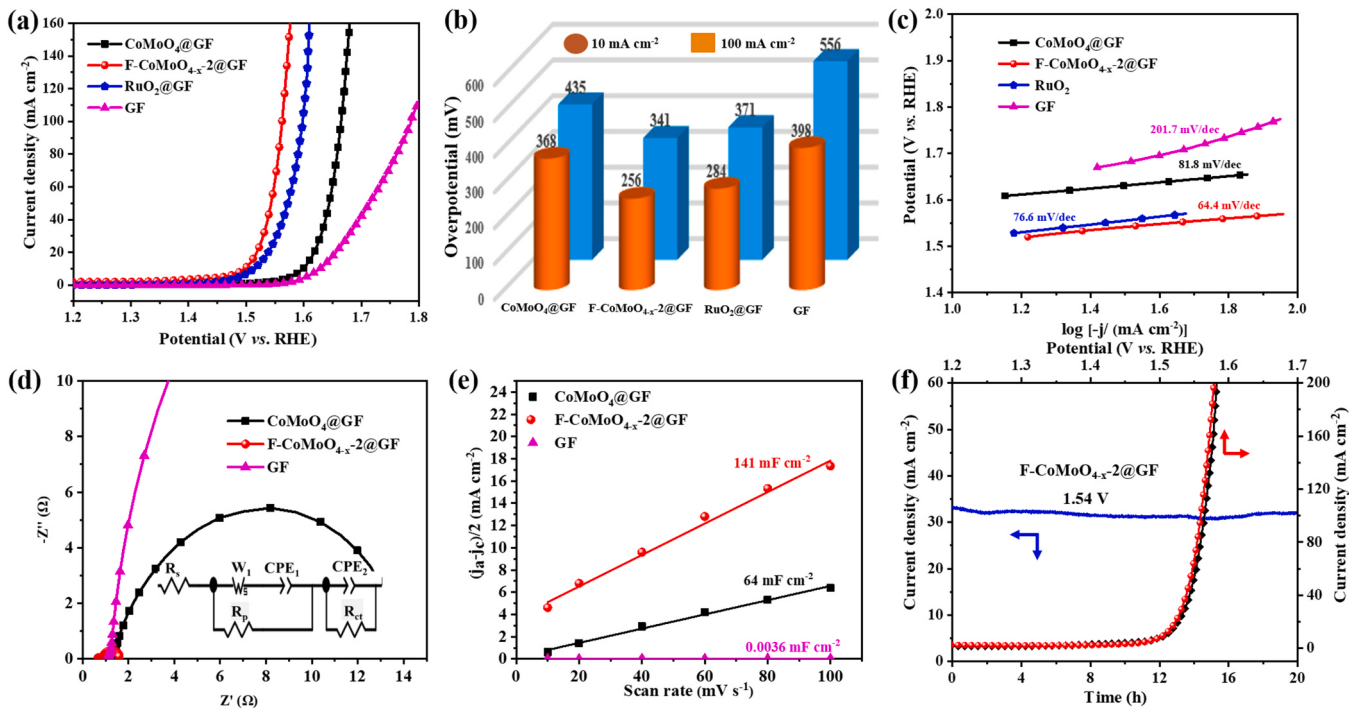


**Fig. 6.** (a) LSV curves, (b) The overpotential of different materials at 10 and 100  $\text{mA cm}^{-2}$  and (c) Tafel plots of  $\text{CoMoO}_4$ @GF,  $\text{F-CoMoO}_{4-x-2}$ @GF,  $\text{RuO}_2$ @GF and GF; (d) Nyquist plots and the corresponding equivalent circuit (inset), and (e)  $C_{dl}$  of  $\text{CoMoO}_4$ @GF,  $\text{F-CoMoO}_{4-x-2}$ @GF and GF at 1.27 V for OER; (f) i-t curves for  $\text{F-CoMoO}_{4-x-2}$ @GF and LSV curves before and after chronoamperometric measurements.

that of O (Fig. S7a) [38].

The Mo 3d spectra of  $\text{CoMoO}_4$ @GF are shown in Fig. 5c. The binding energies of Mo 3d<sub>3/2</sub> (235.74 eV) is 3.11 eV more than that of Mo 3d<sub>5/2</sub> (232.63 eV), which proves the existence of  $\text{Mo}^{6+}$  [39]. After the introduction of F, the binding energies of Mo 3d<sub>5/2</sub> and Mo 3d<sub>3/2</sub> are positively shifted by 1.01 and 0.95 eV, respectively. Interestingly, a new peak appears at 232.96 and 236.19 eV for  $\text{F-CoMoO}_{4-x-2}$ @GF, which is referred to  $\text{Mo}^{5+}$  [40], indicating the formation of low-valence Mo species caused by the fluorine (F) introduction. Moreover, with the increment of F dosage, the peak intensity of  $\text{Mo}^{5+}$  gradually strengthens (Fig. S7b). In F 1s spectrum (Fig. 5d),  $\text{CoMoO}_4$ @GF shows a rough line segment, while for  $\text{F-CoMoO}_{4-x-2}$ @GF, a distinct peak can be found at 685.6 eV, which is attributed to the metal-F bond [41]. As seen from Fig. S7c, the surface atomic percentage of F in  $\text{F-CoMoO}_{4-x-n}$ @GF (Table S1) and the peak density of metal-F bond increase gradually with the F source (dosage) increment. In addition, the O1s spectra of  $\text{CoMoO}_4$ @GF (Fig. 5e) show two characteristic peaks at 530.36 and 531.92 eV attributed to lattice oxygen and oxygen vacancies, respectively [42,43]. After F introduction, the binding energy of lattice oxygen rises slightly from 530.36 eV in  $\text{CoMoO}_4$ @GF to 530.61 eV in  $\text{F-CoMoO}_{4-x-2}$ @GF, and the peak density of oxygen vacancies increases significantly (Fig. S7d).

In order to further demonstrate the existence of oxygen vacancies, EPR test was carried out. As can be distinguished from Fig. 5f,  $\text{F-CoMoO}_{4-x-2}$ @GF displays a strong characteristic peak at  $g = 2.007$  assigned to oxygen vacancies [44,45], indicating that  $\text{F-CoMoO}_{4-x-2}$ @GF contains abundant oxygen vacancies. In contrast, the characteristic peak of EPR of  $\text{CoMoO}_4$  is very weak, indicating less oxygen vacancies. The above results prove that F has been successfully doped into  $\text{CoMoO}_4$  and thus modulates the electronic structure, and then induces abundant oxygen vacancies, which are favorable to accelerating OER catalysis.

### 3.2. Electrochemical characterization

The OER performance of electrocatalysts was estimated by LSV with iR-compensation. Fig. S8a and b show that OER activity of the catalyst is enhanced when F is introduced into  $\text{CoMoO}_4$ , indicating the fluorine-doping as a key factor affecting the performance of OER. Among them,  $\text{F-CoMoO}_{4-x-2}$ @GF (Fluorine content of 2.46% according to XPS results, Table S1) exhibits the best OER performance compared with the other samples synthesized in this work:  $\text{CoMoO}_4$ @GF,  $\text{F-CoMoO}_{4-x-1}$ @GF,  $\text{F-CoMoO}_{4-x-3}$ @GF and  $\text{F-CoMoO}_{4-x-4}$ @GF. Moreover, for comparison reasons,  $\text{CoMoO}_4$ @GF, bare GF, and commercial  $\text{RuO}_2$ @GF were also measured under consistent testing conditions. According to Fig. 6(a, b), bare GF reveals a poor catalytic activity with high overpotential values of 398 and 556 mV at 10 and 100  $\text{mA cm}^{-2}$ , respectively. After the  $\text{CoMoO}_4$  grown on GF, the obtained  $\text{CoMoO}_4$ @GF shows a slight improvement in OER performance, requiring overpotentials of 368 and 435 mV, at 10 and 100  $\text{mA cm}^{-2}$ , respectively. Nonetheless, its OER catalytic activity still remains a big-gap compared with that of commercial  $\text{RuO}_2$ @GF (284 and 371 mV).

After fluorine-doping of  $\text{CoMoO}_4$ , the  $\text{F-CoMoO}_{4-x-2}$ @GF presents the most outstanding OER performance and requires overpotentials of only 256 and 341 mV at 10 and 100  $\text{mA cm}^{-2}$ , respectively, which is 112 mV lower than that of  $\text{CoMoO}_4$ @GF at 10  $\text{mA cm}^{-2}$  and also outperforms that of  $\text{RuO}_2$ @GF. In addition, two LSV curves obtained for pure GF and F-doped GF substantially coincide (Fig. S9), suggesting no obvious OER improvement after F doping into pure GF. This result indicates that  $\text{CoMoO}_4$  is the true catalytic center and eliminates the interference of GF substrate. Moreover, it is worth noting that  $\text{F-CoMoO}_{4-x-2}$ @GF has better OER performance than the majority of recently reported TMOs (Table S2).

To get insight into the mechanism of OER, the Tafel slope is carefully calculated according to the corresponding LSV curves. In general, OER process typically consists of the following four steps [46]:



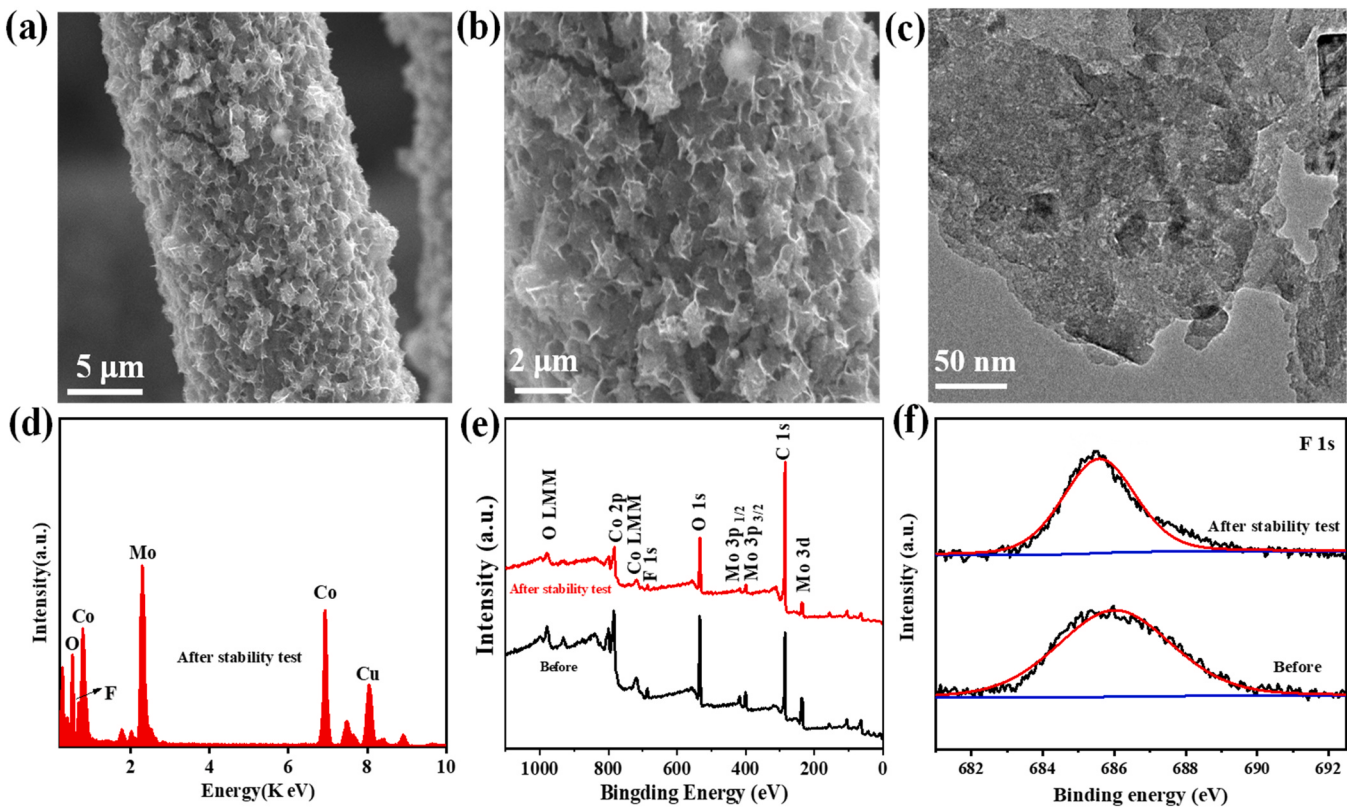
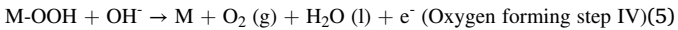
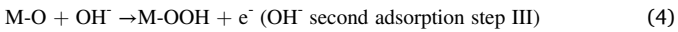
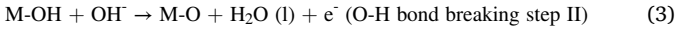


**Fig. 7.** (a, b) SEM images of F-CoMoO<sub>4-x</sub>-2@GF after stability test; (c) TEM images and (d) STEM-EDS spectra images of F-CoMoO<sub>4-x</sub>-2 after stability test; (e) XPS spectra and (f) F 1s of F-CoMoO<sub>4-x</sub>-2@GF before and after OER stability test at an applied potential of 1.54 V for 20 h.



The slopes of Tafel plots of reactions (2), (3), and (5) correspond to 120, 30, and 20 mV dec<sup>-1</sup>, respectively [47]. It should be noted that, except for GF, the Tafel slopes of CoMoO<sub>4</sub>@GF, F-CoMoO<sub>4-x</sub>-2@GF, and RuO<sub>2</sub>@GF are all in the range of 30–120 mV dec<sup>-1</sup> (Fig. 6c), showing that the rate-controlling steps may be jointly determined by the first adsorption of OH<sup>-</sup> step I (Eq. (2)) and the O-H bond breakage step II (Eq. (3)) [48]. From Fig. 6c, the Tafel slope for F-CoMoO<sub>4-x</sub>-2@GF (64.4 mV dec<sup>-1</sup>) is smaller than that of GF (201.7 mV dec<sup>-1</sup>), RuO<sub>2</sub>@GF (76.6 mV dec<sup>-1</sup>), and CoMoO<sub>4</sub>@GF (81.8 mV dec<sup>-1</sup>), suggesting the promoted first adsorption of OH<sup>-</sup> and the O-H bond breakage process. This could be due to the fact that F doping modulates the electronic structure of the active sites and provides more oxygen vacancies. Specially, the oxygen vacancies of F-CoMoO<sub>4-x</sub>-2@GF could further change the electronic properties of the surface and form distorted structure, which facilitates the adsorption of OH<sup>-</sup> at the F-CoMoO<sub>4-x</sub>-2@GF surface [49]. Thus, the OER catalytic kinetics is efficiently boosted. Meanwhile, compared with CoMoO<sub>4</sub>@GF (81.8 mV dec<sup>-1</sup>), F-CoMoO<sub>4-x</sub>-1@GF (64.8 mV dec<sup>-1</sup>), F-CoMoO<sub>4-x</sub>-3@GF (65.3 mV dec<sup>-1</sup>) and F-CoMoO<sub>4-x</sub>-4@GF (71.5 mV dec<sup>-1</sup>) in Fig. S8c, the Tafel slope of F-CoMoO<sub>4-x</sub>-2@GF is also the lowest, confirming an optimized F doping, which indicates that F-CoMoO<sub>4-x</sub>-2@GF has the fastest OER kinetics and thus shows the best OER performance.

The catalytic kinetics information of OER can be obtained from EIS. Usually, the charge transfer resistance ( $R_{ct}$ ) can be obtained by fitting a semicircular curve at the intersection of low frequency and x-axis. Fig. 6d represents the Nyquist plots of obtained materials at an applied potential of 0.65 V and corresponding equivalent circuit (inset of Fig. 6d). As calculated according to the Figs. 6d, S10 and summarized

results in Table S3, the  $R_{ct}$  of CoMoO<sub>4</sub>@GF (2.617  $\Omega$ ) can be even reduced to 0.520  $\Omega$  after F doping. Moreover, the  $R_{ct}$  of F-CoMoO<sub>4-x</sub>-2@GF (0.520  $\Omega$ ) is smaller than those of F-CoMoO<sub>4-x</sub>-1@GF (0.922  $\Omega$ ), F-CoMoO<sub>4-x</sub>-3@GF (0.982  $\Omega$ ), F-CoMoO<sub>4-x</sub>-4@GF (1.491  $\Omega$ ). The lower  $R_{ct}$  value is beneficial for the rapid charge transfer, thus speeding up the OER dynamic process of F-CoMoO<sub>4-x</sub>-n@GF. Meanwhile, the solution resistance ( $R_s$ ) of F-CoMoO<sub>4-x</sub>-2@GF drops to 0.578  $\Omega$  after F introduction, indicating that F doping is favorable to improve the conductivity. This could be due to the fact that F introduction optimizes the electronic structure of CoMoO<sub>4</sub> and then improves its conductivity. The ECSA can evaluate the amount of catalytically active sites, which is proportional to the double-layer capacitance ( $C_{dl}$ ) [50]. Accordingly, the larger  $C_{dl}$  implies more catalytically active sites.

As clearly shown in Figs. 6e, S11 and S12, F-CoMoO<sub>4-x</sub>-2@GF presents a larger  $C_{dl}$  (141 mF cm<sup>-2</sup>) compared with those of CoMoO<sub>4</sub>@GF (64 mF cm<sup>-2</sup>), GF (0.0036 mF cm<sup>-2</sup>), F-CoMoO<sub>4-x</sub>-1@GF (129 mF cm<sup>-2</sup>), F-CoMoO<sub>4-x</sub>-3@GF (119 mF cm<sup>-2</sup>) and F-CoMoO<sub>4-x</sub>-4@GF (107 mF cm<sup>-2</sup>), suggesting more catalytically active sites for F-CoMoO<sub>4-x</sub>-2@GF, which benefits the OER process.

### 3.3. Stability tests

Stability is a critical evaluation factor in relation to large-scale applications. Thus, current-time (i-t) curve was obtained to estimate the stability of F-CoMoO<sub>4-x</sub>-2@GF. Fig. 6f displays that i-t curve has no significant decay for 20 h at an applied potential of 1.54 V, revealing that F-CoMoO<sub>4-x</sub>-2@GF possesses a superior durability in OER process. The corresponding LSV curves (Fig. 6f) of F-CoMoO<sub>4-x</sub>-2@GF changes slightly before and after 20 h stability test, also indicating a good stability of F-CoMoO<sub>4-x</sub>-2@GF for OER.

In order to further study the change of components and morphology

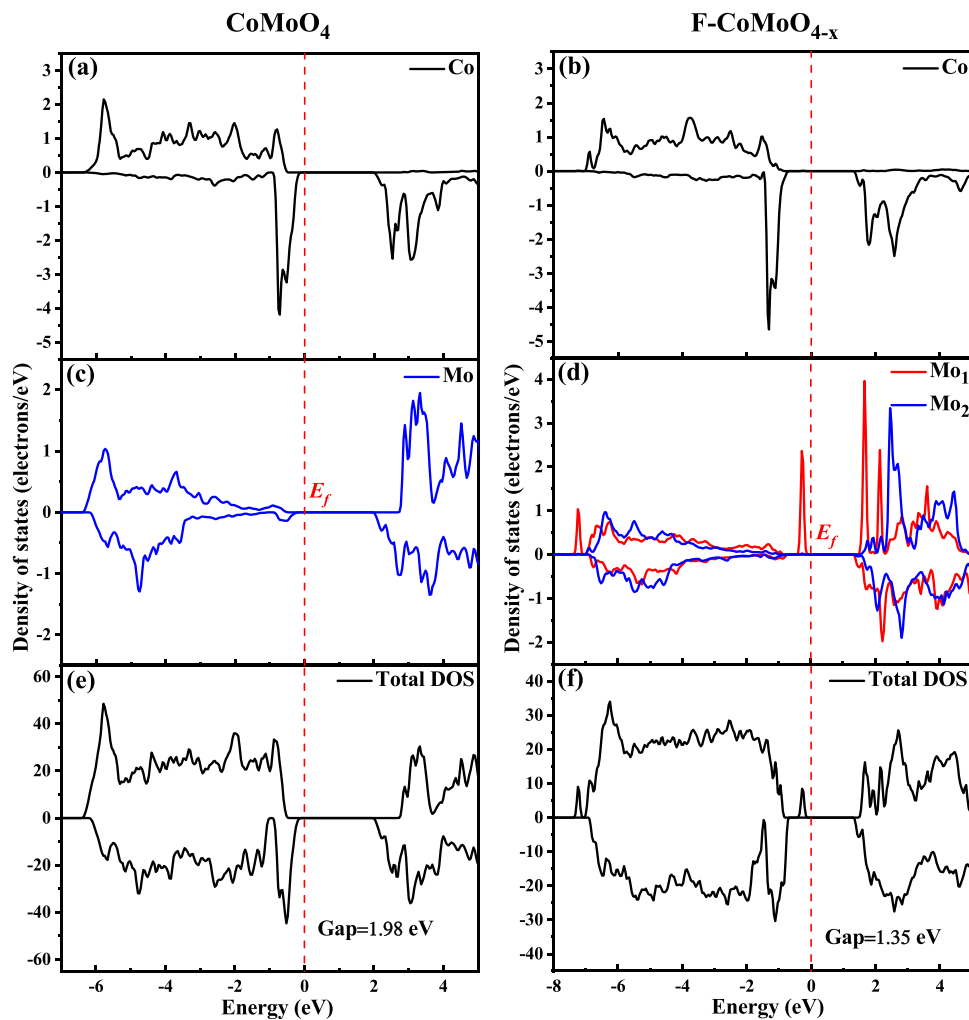


**Fig. 8.** Co 3d density of states (DOS) in (a) CoMoO<sub>4</sub> and (b) F-CoMoO<sub>4-x</sub>; Mo 4d DOS in (c) CoMoO<sub>4</sub> and (d) F-CoMoO<sub>4-x</sub>; Total DOS of (e) CoMoO<sub>4</sub> and (f) F-CoMoO<sub>4-x</sub>.

of the catalyst after the OER stability tests, SEM, TEM, EDS and XPS characterizations were carried out for the used F-CoMoO<sub>4-x</sub>-2@GF samples. As seen from Fig. 7(a, b), the morphology does not change substantially, but some agglomerations appear, which could be caused by the fact that the electrode surface has been repeatedly collided by O<sub>2</sub> bubbles in the process of OER, leading to the collapse in part of sample structure. In addition, the nanosheets structure is well maintained (Fig. 7c) and F element still exists in CoMoO<sub>4</sub> after the stability test (Fig. 7d).

Meanwhile, the XPS full spectra (Fig. 7e) and F 1s spectrum (Fig. 7f) further confirm the existence of F with 2.25 at% surface atomic percentage according to XPS result (Table S1) after the stability test. Fig. S13a-c shows that there is almost no change for both phase structure and composition after the stability test, proving that F-CoMoO<sub>4-x</sub>-2@GF has good structural stability, and thus presents excellent performance stability.

#### 3.4. DFT calculations

To get insight into the reason for the improvement in OER performance of the catalyst, the density of states (DOS) of pure CoMoO<sub>4</sub> and F-CoMoO<sub>4-x</sub> were further calculated by DFT calculation. According to the XRD results, we establish the atomic structure model of  $\beta$ -CoMoO<sub>4</sub>, in which Co<sup>2+</sup> and Mo<sup>6+</sup> are coordinated with six and four oxygen atoms, respectively (Fig. S14a and c). From the analysis of XPS and EPR results, considering F introduction and the generated oxygen vacancies, the

atomic structure model of fluorine-doped CoMoO<sub>4</sub> (F-CoMoO<sub>4-x</sub>) has been further constructed (Fig. S14b and d). According to Fig. S14e and f derived from the local views of CoMoO<sub>4</sub> and F-CoMoO<sub>4-x</sub>, after structure optimization, it can be seen that after F introduction, most bond lengths between molybdenum atom and oxygen atom increase, and thus the bond energy of Mo-O bonds weakens accompanied by a positive shift in the position of binding energy, which is due to the strong electronegativity of F and consistent with the Mo peak shift from the XPS result.

The effect of F introduction in CoMoO<sub>4</sub> was analyzed by DOS. By comparing the electron structure of Co 3d in Fig. 8(a, b), it can be found that both belong to  $t_{2g}^3(\uparrow) e_g^2(\uparrow) t_{2g}^2(\downarrow)$  for CoMoO<sub>4</sub> and F-CoMoO<sub>4-x</sub>, illustrating that the oxidation state of Co atom is always +2, which indicates that the introduction of F does not substantially change the oxidation state of Co atoms. However, the electronic structure of Mo-4d states changes to a certain extent. In CoMoO<sub>4</sub> (Fig. 8c), Mo atoms exist in the form of Mo<sup>6+</sup> and have no magnetic moments. While, in F-CoMoO<sub>4-x</sub> (Fig. 8d), it can be found that there is part of filled Mo-4d orbital below the Fermi level, which shows the reduction of Mo atoms adjacent to O vacancies. In this case, the corresponding magnetic moment becomes  $1 \mu\text{B}$ , belonging to Mo<sup>5+</sup>, which agrees well with the XPS results.

The total DOS (Fig. 8(e, f)) shows that after F introduction, the energy gap of CoMoO<sub>4</sub> decreases from 1.98 to 1.35 eV, and thus the electrical conductivity is improved. Consequently, the band gap decreases through the change of Mo-4d states because of F doping and O vacancies, resulting in favorable OER catalytic activity.

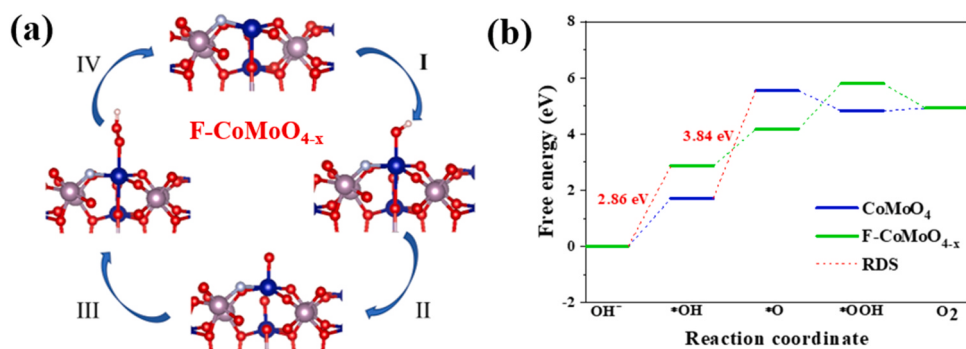


**Fig. 9.** (a) Four intermediates of F-CoMoO<sub>4-x</sub> based on CoMoO<sub>4</sub> model (002) crystal plane after F doped; (b) Free-energy diagrams for F-CoMoO<sub>4-x</sub> and CoMoO<sub>4</sub>.

To further elucidate the reaction mechanism, the free energy of the four-electron OER process was calculated to confirm the rate-determining step (RDS). Two models including the CoMoO<sub>4</sub> and F-CoMoO<sub>4-x</sub> were used to investigate the OER process. Fig. 9a shows four intermediates of F-CoMoO<sub>4-x</sub>, which are established by using a F atom to replace an O atom located in the CoMoO<sub>4</sub> (002) plane. According to the calculated models' free energy of the four steps reactions for CoMoO<sub>4</sub> and F-CoMoO<sub>4-x</sub>, it is found that the formation of \*O from \*OH requires the largest free energy ( $\Delta G_2 = 3.84$  eV) for the CoMoO<sub>4</sub>, showing that the Step II is the RDS of the OER (Fig. 9b).

However, when F atom is introduced into the structure surface, the free energy of \*OH and \*O can be greatly influenced and the RDS is Step I ( $\Delta G_1 = 2.86$  eV) for F-CoMoO<sub>4-x</sub> (Fig. 9b). This lower energy-cost RDS reveals F-CoMoO<sub>4-x</sub> possesses the faster OER than CoMoO<sub>4</sub>. DFT results confirm that the introducing of F not only reduce the bandgap to speed up the electron transfer, but also optimize the OER free energy, resulting in favorable OER catalytic activity.

#### 4. Conclusions

In summary, we have demonstrated that fluorine doping of CoMoO<sub>4</sub> nanosheet arrays on GF as electrocatalyst can efficiently promote OER catalytic activity. Experimental and theoretical studies prove that fluorine-doped CoMoO<sub>4</sub> nanosheets can induce the formation of rich oxygen vacancies, optimize the electronic configuration, decrease the energy band gap, promote the electrical conductivity, optimize the OER free energy and thus enhance intrinsic OER activity of CoMoO<sub>4</sub>. Therefore, the optimized F-CoMoO<sub>4-x</sub>-2@GF sample exhibits an excellent OER activity with an overpotential of 256 mV at 10 mA cm<sup>-2</sup> and a Tafel slope of 64.4 mV dec<sup>-1</sup>, superior to that of RuO<sub>2</sub>@GF. Importantly, the proposed fluorine-doping protocol may open a new way for other transition metal oxides electrocatalysts toward water splitting.

#### CRediT authorship contribution statement

**Weiwei Xie:** Investigation, Formal analysis, Data curation, Validation, Writing – original draft. **Jianhao Huang:** Investigation, Validation, Data curation. **Liting Huang:** Methodology, Validation, Investigation. **Shipeng Geng:** Validation, Data curation, Visualization. **Shuqin Song:** Conceptualization, Supervision, Project administration, Funding acquisition, Writing – review & editing. **Panagiotis Tsiakaras:** Conceptualization, Methodology, Writing – review & editing. **Yi Wang:** Conceptualization, Methodology, Supervision, Funding acquisition, Writing – review & editing.

#### Declaration of Competing Interest

The authors declare that they have no known competing financial interests or personal relationships that could have appeared to influence the work reported in this paper.

#### Acknowledgments

Authors are grateful for financial support to: National Natural Science Foundation of China (21975292, 21978331, 21905311), China; Training Program of the Major Research Plan of the National Natural Science Foundation of China (90261124), China; Guangdong Basic and Applied Basic Research Foundation (2021A1515010167, 2020A1515010343), the Fundamental Research Fund for the Central Universities (Nos. 19lgpy136, 19lgpy116), China. Prof. Tsiakaras thankfully acknowledges co-financing by European Union & Greek National Funds through the Operational Program Competitiveness, Entrepreneurship and Innovation, under the call RESEARCH – CREATE-INNOVATE (T1EDK-02442), EU & Greece.

#### Appendix A. Supplementary material

Supplementary data associated with this article can be found in the online version at doi:10.1016/j.apcatb.2021.120871.

#### References

- [1] V.R. Stamenkovic, D. Strmcnik, P.P. Lopes, N.M. Markovic, Energy and fuels from electrochemical interfaces, *Nat. Mater.* 16 (2017) 57–69, <https://doi.org/10.1038/nmat4738>.
- [2] Y. Jiao, Y. Zheng, M. Jaroniec, S. Qiao, Design of electrocatalysts for oxygen- and hydrogen-involving energy conversion reactions, *Chem. Soc. Rev.* 44 (2015) 2060–2086, <https://doi.org/10.1039/C4CS00470A>.
- [3] Y. Shi, B. Zhang, Recent advances in transition metal phosphide nanomaterials: synthesis and applications in hydrogen evolution reaction, *Chem. Soc. Rev.* 45 (2016) 1529–1541, <https://doi.org/10.1039/C6CS0013E>.
- [4] Y. Wang, G. Qian, Q. Xu, H. Zhang, F. Shen, L. Luo, S. Yin, Industrially promising IrNi-FeNi<sub>3</sub> hybrid nanosheets for overall water splitting catalysis at large current density, *Appl. Catal. B Environ.* 286 (2021), 119881, <https://doi.org/10.1016/j.apcatb.2021.119881>.
- [5] M.G. Walter, E.L. Warren, J.R. McKone, S.W. Boettcher, Q. Mi, E.A. Santori, N. S. Lewis, Solar water splitting cells, *Chem. Rev.* 110 (2010) 6446–6473, <https://doi.org/10.1021/cr1002326>.
- [6] P.G. Bruce, S.A. Freunberger, L.J. Hardwick, T. Jean-Marie, Hardwick, Li-O<sub>2</sub> and Li-S batteries with high energy storage, *Nat. Mater.* 11 (2012) 19–29, <https://doi.org/10.1038/nmat3191>.
- [7] K.A. Stoerzinger, O. Diaz-Morales, M. Kolb, R. Rao, R. Frydendal, L. Qiao, X. R. Wang, N.B. Halck, J. Rossmeisl, H.A. Hansen, T. Vegge, I.E.L. Stephens, M.T. M. Koper, Y. Shao-Horn, Orientation-dependent oxygen evolution on RuO<sub>2</sub> without lattice exchange, *ACS Energy Lett.* 2 (2017) 876–881, <https://doi.org/10.1021/acsenergylett.7b00135>.
- [8] Y. Zhang, J. Fu, H. Zhao, R. Jiang, F. Tian, R. Zhang, Tremella-like Ni<sub>3</sub>S<sub>2</sub>/MnS with ultrathin nanosheets and abundant oxygen vacancies directly used for high speed overall water splitting, *Appl. Catal. B Environ.* 257 (2019), 117899, <https://doi.org/10.1016/j.apcatb.2019.117899>.
- [9] Z. Li, M. Zheng, X. Zhao, J. Yang, W. Fan, Synergistic engineering of architecture and composition in Ni<sub>x</sub>Co<sub>1-x</sub>Mo<sub>4</sub>@CoMoO<sub>4</sub> nanobrush arrays towards efficient overall water splitting electrocatalysis, *Nanoscale* 11 (2019) 22820–22831, <https://doi.org/10.1039/C9NR08281F>.
- [10] Y. Ding, B.Q. Miao, Y.C. Jiang, H.C. Yao, X.F. Li, Y. Chen, Polyethylenimine-modified nickel phosphide nanosheets: interfacial protons boost the hydrogen evolution reaction, *J. Mater. Chem. A* 7 (2019) 13770–13776, <https://doi.org/10.1039/C9TA04283K>.
- [11] D.R. Kauffman, X.Y. Deng, D.C. Sorescu, T.-D. Nguyen-Phan, C. Wang, C.M. Marin, E. Stavitski, I. Waluyo, A. Hunt, Edge-enhanced oxygen evolution reactivity at

ultrathin, Au-supported  $\text{Fe}_2\text{O}_3$  electrocatalysts, *ACS Catal.* 9 (2019) 5375–5382, <https://doi.org/10.1021/acscatal.9b01093>.

[12] H. Liao, X. Guo, Y. Hou, H. Liang, Z. Zhou, H. Yang, Construction of defect-rich Ni-Fe-doped  $\text{K}_{0.23}\text{MnO}_2$  cubic nanoflowers via etching prussian blue analogue for efficient overall water splitting, *Small* 16 (2020), 1905223, <https://doi.org/10.1002/smll.201905223>.

[13] C. Kuai, Y. Zhang, L. Han, H. Xin, C.-J. Sun, F. Lin, Creating compressive stress at the  $\text{NiOOH}/\text{NiO}$  interface for water oxidation, *J. Mater. Chem. A* 8 (2020) 10747–10754, <https://doi.org/10.1039/D0TA04244G>.

[14] R.M. Ramsundar, V.K. Pillai, P.A. Joy, Spin state engineered  $\text{Zn}_x\text{Co}_{3-x}\text{O}_4$  as an efficient oxygen evolution electrocatalyst, *Phys. Chem. Chem. Phys.* 20 (2018) 29452–29461, <https://doi.org/10.1039/C8CP06641H>.

[15] Z.X. Yin, S. Zhang, W. Chen, X.Z. Ma, Z. Yang, Z.F. Zhang, W. Xin, J.L. Li, Hybrid-atom-doped  $\text{NiMoO}_4$  nanotubes for oxygen evolution reaction, *New J. Chem.* 44 (2020) 17477–17482, <https://doi.org/10.1039/D0NJ02305A>.

[16] R. Li, Y. Guo, H. Chen, K. Wang, R. Tan, B. Long, Y. Tong, P. Tsikararas, S. Song, Y. Wang, Anion-cation double doped  $\text{Co}_3\text{O}_4$  microtube architecture to promote high-valence Co species formation for enhanced oxygen evolution reaction, *ACS Sustain. Chem. Eng.* 7 (2019) 11901–11910, <https://doi.org/10.1021/acssuschemeng.9b02558>.

[17] Y. Liang, H. Wang, J. Zhou, Y. Li, J. Wang, T. Regier, H. Dai, Covalent hybrid of spinel manganese-cobalt oxide and graphene as advanced oxygen reduction electrocatalysts, *J. Am. Chem. Soc.* 134 (2012) 3517–3523, <https://doi.org/10.1021/ja210924t>.

[18] T.Y. Ma, S. Dai, M. Jaroniec, S.Z. Qiao, Metal-organic framework derived hybrid  $\text{Co}_3\text{O}_4$ -carbon porous nanowire arrays as reversible oxygen evolution electrodes, *J. Am. Chem. Soc.* 136 (2014) 13925–13931, <https://doi.org/10.1021/ja5082553>.

[19] L. An, J. Feng, Y. Zhang, R. Wang, H. Liu, G.-C. Wang, F. Cheng, P. Xi, Epitaxial heterogeneous interfaces on  $\text{N}-\text{NiMoO}_4/\text{NiS}_2$  nanowires/nanosheets to boost hydrogen and oxygen production for overall water splitting, *Adv. Funct. Mater.* 29 (2019), 1805298, <https://doi.org/10.1002/adfm.201805298>.

[20] Z. Liu, C. Yuan, F. Teng, Crystal facets-predominated oxygen evolution reaction activity of earth abundant  $\text{CoMoO}_4$  electrocatalyst, *J. Alloy. Compd.* 781 (2019) 460–466, <https://doi.org/10.1016/j.jallcom.2018.12.026>.

[21] H.-S. Jiang, Z. Cui, C.-T. Xu, W.-Y. Li, Humid atmospheric pressure plasma jets exposed micro-defects on  $\text{CoMoO}_4$  nanosheets with enhanced OER performance, *Chem. Commun.* 55 (2019) 9432–9435, <https://doi.org/10.1039/C9CC04493K>.

[22] B. Fei, Z.-L. Chen, Y. Ha, R.-R. Wang, H. Yang, Y.-H. Xu, R.-B. Wu, Anion-cation co-substitution activation of spinel  $\text{CoMoO}_4$  for efficient oxygen evolution reaction, *Chem. Eng. J.* 394 (2020), 124926, <https://doi.org/10.1016/j.cej.2020.124926>.

[23] F. Lai, J. Feng, X. Ye, W. Zong, G. He, Y.-E. Miao, X. Han, X.Y. Ling, I.P. Parkin, B. Pan, Y. Sun, T. Liu, Energy level engineering in transition-metal doped spinel-structured nanosheets for efficient overall water splitting, *J. Mater. Chem. A* 7 (2019) 827–833, <https://doi.org/10.1039/C8TA10162K>.

[24] K. Chi, X. Tian, Q.-J. Wang, Z.-Y. Zhang, Oxygen vacancies engineered  $\text{CoMoO}_4$  nanosheet arrays as efficient bifunctional electrocatalysts for overall water splitting, *J. Catal.* 381 (2020) 44–52, <https://doi.org/10.1016/j.jcat.2019.10.025>.

[25] Z. Liu, C. Yuan, F. Teng, Crystal facets-predominated oxygen evolution reaction activity of earth abundant  $\text{CoMoO}_4$  electrocatalyst, *J. Alloy. Compd.* 781 (2019) 460–466, <https://doi.org/10.1016/j.jallcom.2018.12.026>.

[26] Y. Gong, Z. Yang, Y. Lin, J. Wang, H. Pan, Z. Xu, Hierarchical heterostructure  $\text{NiCo}_2\text{O}_4/\text{CoMoO}_4/\text{NF}$  as an efficient bifunctional electrocatalyst for overall water splitting, *J. Mater. Chem. A* 6 (2018) 16950–16958, <https://doi.org/10.1039/C8TA04325F>.

[27] Z.-H. Xiao, C. Xie, Y.-Y. Wang, R. Chen, S.-Y. Wang, Recent advances in defect electrocatalysts: preparation and characterization, *J. Energy Chem.* 53 (2021) 208–225, <https://doi.org/10.1016/j.jechem.2020.04.063>.

[28] Z.-C. Wang, H.-L. Liu, R.-X. Ge, X. Ren, J. Ren, D.-J. Yang, L.-X. Zhang, Phosphorus-doped  $\text{Co}_3\text{O}_4$  nanowire array: a highly efficient bifunctional electrocatalyst for overall water splitting, *ACS Catal.* 8 (2018) 2236–2241, <https://doi.org/10.1021/acscatal.7b03544>.

[29] L. Xu, Z.-M. Wang, J.-L. Wang, Z.-H. Xiao, X.-B. Huang, Z.-G. Liu, S.-Y. Wang, N-doped nanoporous  $\text{Co}_3\text{O}_4$  nanosheets with oxygen vacancies as oxygen evolving electrocatalysts, *Nanotechnology* 28 (2017), 242501, <https://doi.org/10.1088/1361-6528/aa6381>.

[30] Y. Liu, X. Hua, C. Xiao, T. Zhou, P. Huang, Z. Guo, B. Pan, Y. Xie, Heterogeneous spin states in ultrathin nanosheets induce subtle lattice distortion to trigger efficient hydrogen evolution, *J. Am. Chem. Soc.* 138 (2016) 5087–5092, <https://doi.org/10.1021/jacs.6b00858>.

[31] Y. Wang, T. Zhou, K. Jiang, P. Da, Z. Peng, J. Tang, B. Kong, W.-B. Cai, Z. Yang, G. Zheng, Reduced mesoporous  $\text{Co}_3\text{O}_4$  nanowires as efficient water oxidation electrocatalysts and supercapacitor electrodes, *Adv. Energy Mater.* 4 (2014), 1400696, <https://doi.org/10.1002/aenm.201400696>.

[32] W.-J. He, L.-L. Han, Q.-Y. Hao, X.-R. Zheng, Y. Li, J. Zhang, C.-C. Liu, H.-L. Xin, Fluorine-anion-modulated electron structure of nickel sulfide nanosheet arrays for alkaline hydrogen evolution, *ACS Energy Lett.* 4 (2019) 2905–2912, <https://doi.org/10.1021/acsenergylett.9b02316>.

[33] K. Xu, Y.-Q. Sun, X.-L. Li, Z.-H. Zhao, Y.-Q. Zhang, C.-C. Li, H.-J. Fan, Fluorine-induced dual defects in cobalt phosphide nanosheets enhance hydrogen evolution reaction activity, *ACS Mater. Lett.* 2 (2020) 736–743, <https://doi.org/10.1021/acsmaterialslett.0c00209>.

[34] S.-D. Liu, Y. Yin, D.-X. Ni, K.-S. Hui, S.-C. Lee, C.-Y. Ouyang, S.-C. Jun, Phosphorous-containing oxygen-deficient cobalt molybdate as an advanced electrode material for supercapacitors, *Energy Storage Mater.* 19 (2019) 186–196, <https://doi.org/10.1016/j.ensm.2018.10.022>.

[35] Y. Pan, Y. Lin, Y. Chen, Y. Liu, C. Liu, Cobalt phosphide-based electrocatalysts: synthesis and phase catalytic activity comparison for hydrogen evolution, *J. Mater. Chem. A* 4 (2016) 4745–4754, <https://doi.org/10.1039/C6TA00575F>.

[36] R. Li, B. Hu, T. Yu, H. Chen, Y. Wang, S. Song, Insights into correlation among surface-structure-activity of cobalt-derived pre-catalyst for oxygen evolution reaction, *Adv. Sci.* 7 (2019), 1902830, <https://doi.org/10.1002/advs.201902830>.

[37] J. Zhao, H. Li, C. Li, Q. Zhang, J. Sun, X. Wang, J. Guo, L. Xie, J. Xie, B. He, MOF for template-directed growth of well-oriented nanowire hybrid arrays on carbon nanotube fibers for wearable electronics integrated with triboelectric nanogenerators, *Nano Energy* 45 (2018) 420–431, <https://doi.org/10.1016/j.nanoen.2018.01.021>.

[38] X. Zhang, F. Meng, S. Mao, Q. Ding, M.J. Shearer, M.S. Faber, J. Chen, R.J. Hamers, S. Jin, Amorphous  $\text{MoS}_x\text{Cl}_y$  electrocatalyst supported by vertical graphene for efficient electrochemical and photoelectrochemical hydrogen generation, *Energy Environ. Sci.* 8 (2015) 862–868, <https://doi.org/10.1039/C4EE03240C>.

[39] J. Meng, J. Fu, X. Yang, M. Wei, S. Liang, H.-Y. Zang, H. Tan, Y. Wang, Y. Li, Efficient  $\text{MMoO}_4$  ( $\text{M} = \text{Co, Ni}$ ) carbon cloth electrodes for water oxidation, *Inorg. Chem. Front.* 4 (2017) 1791–1797, <https://doi.org/10.1039/C7QJ00435D>.

[40] M. Vasilopoulou, A.M. Douvas, D.G. Georgiadou, L.C. Palilis, S. Kennou, L. Sygellou, A. Soulatis, I. Kostis, G. Papadimitropoulos, D. Davatzoglou, P. Argitis, The influence of hydrogenation and oxygen vacancies on molybdenum oxides work function and gap states for application in organic optoelectronics, *J. Am. Chem. Soc.* 134 (2012) 16178–16187, <https://doi.org/10.1021/ja3026906>.

[41] J. Tan, L. Liu, S. Guo, H. Hu, Z. Yan, Q. Zhou, Z. Huang, H. Shu, X. Yang, X. Wang, The electrochemical performance and mechanism of cobalt (II) fluoride as anode material for lithium an sodium ion batteries, *Electrochim. Acta* 168 (2015) 225–233, <https://doi.org/10.1016/j.electacta.2015.04.029>.

[42] F. Wu, Q. Liao, F. Cao, L. Li, Y. Zhang, Non-noble bimetallic  $\text{NiMoO}_4$  nanosheets integrated Si photoanodes for highly efficient and stable solar water splitting, *Nano Energy* 34 (2017) 8–14, <https://doi.org/10.1016/j.nanoen.2017.02.004>.

[43] L. Xu, Q. Jiang, Z. Xiao, X. Li, J. Huo, S. Wang, L. Dai, Plasma-engraved  $\text{Co}_3\text{O}_4$  nanosheets with oxygen vacancies and high surface area for the oxygen evolution reaction, *Angew. Chem. Int. Ed.* 128 (2016) 5363–5367, <https://doi.org/10.1002/anie.201600687>.

[44] R. Yang, X. Lu, X. Huang, Z. Chen, X. Zhang, M. Xu, Q. Song, L. Zhu, Bi-component  $\text{Cu}_2\text{O}-\text{CuCl}$  composites with tunable oxygen vacancies and enhanced photocatalytic properties, *Appl. Catal. B Environ.* 170 (2015) 225–232, <https://doi.org/10.1016/j.apcatb.2015.01.046>.

[45] K. Wang, J.-H. Huang, H.-X. Chen, Y. Wang, S.-Q. Song, Recent advances in electrochemical 2e oxygen reduction reaction for on-site hydrogen peroxide production and beyond, *Chem. Commun.* 56 (2020) 12109–12121, <https://doi.org/10.1039/D0CC05156J>.

[46] N.-T. Stuen, S.-F. Hung, Q. Quan, N. Zhang, Y.-J. Xu, H.-M. Chen, Electrocatalysis for the oxygen evolution reaction: recent development and future perspectives, *Chem. Soc. Rev.* 46 (2017) 337–365, <https://doi.org/10.1039/C6CS00328A>.

[47] T. Shinagawa, A.T. Garcia-Esparza, K. Takanabe, Insight on Tafel slopes from a microkinetic analysis of aqueous electrocatalysis for energy conversion, *Sci. Rep.* 5 (2015) 13801, <https://doi.org/10.1038/srep13801>.

[48] G. Zhang, H. Wang, J. Yang, Q. Zhao, L. Yang, H. Tang, C. Liu, H. Chen, Y. Lin, F. Pan, Temperature effect on Co-based catalysts in oxygen evolution reaction, *Inorg. Chem.* 57 (2018) 2766–2772, <https://doi.org/10.1021/acs.inorgchem.7b03168>.

[49] X. Zhang, X. Li, R. Li, Y. Lu, S. Song, Y. Wang, Highly active core-shell carbon/ $\text{NiCo}_2\text{O}_4$  double microtubes for efficient oxygen evolution reaction: ultralow overpotential and superior cycling stability, *Small* 15 (2019), 1903297, <https://doi.org/10.1002/smll.201903297>.

[50] Z. Kang, H. Guo, J. Wu, X. Sun, Z. Zhang, Q. Liao, S. Zhang, H. Si, P. Wu, L. Wang, Y. Zhang, Engineering an earth-abundant element-based bifunctional electrocatalyst for highly efficient and durable overall water splitting, *Adv. Funct. Mater.* 29 (2019), 1807031, <https://doi.org/10.1002/adfm.201807031>.